nature materials

SUPPLEMENTARY INFORMATION

DOI: 10.1038/NMAT3810

Local Electrostatic Imaging of Striped Domain Order in $LaAlO_3/SrTiO_3$

M. Honig*[1], J. A. Sulpizio*[1], J. Drori[1], A. Joshua[1], E. Zeldov[1], and S. Ilani[1]

[1]*Department of Condensed Matter Physics, Weizmann Institute of Science, Rehovot 76100, Israel.*

* These authors contributed equally to this work

DOI: 10.1038/NMAT3810

S1. SEM images of the scanning SET probe

A scanning electron microscope (SEM) image of a typical nanotube-based single electron transistor (SET) device is shown in Fig. S1. The SET is situated at the edge of a narrow $(\sim 10\mu m)$ and tall $(\sim 100\mu m)$ cantilever-like pillar, etched in silicon. On this pillar we pattern contact electrodes (yellow, inset Fig S1) and gate electrodes (blue, inset Fig S1) using electron beam lithography. On a separate chip we grow many parallel nanotubes suspended across wide trenches $(\sim 100\mu m)$. We then mate[1] the two chips to place an individual semiconducting nanotube at the pillar's leading edge, as shown in the inset (indicated by black arrows). After mating the nanotube is electrically connected to the source and drain contacts (yellow) and is suspended above multiple gate electrodes (blue). For the current experiments we electrically chain all the gate electrodes together, having them act as a single gate.

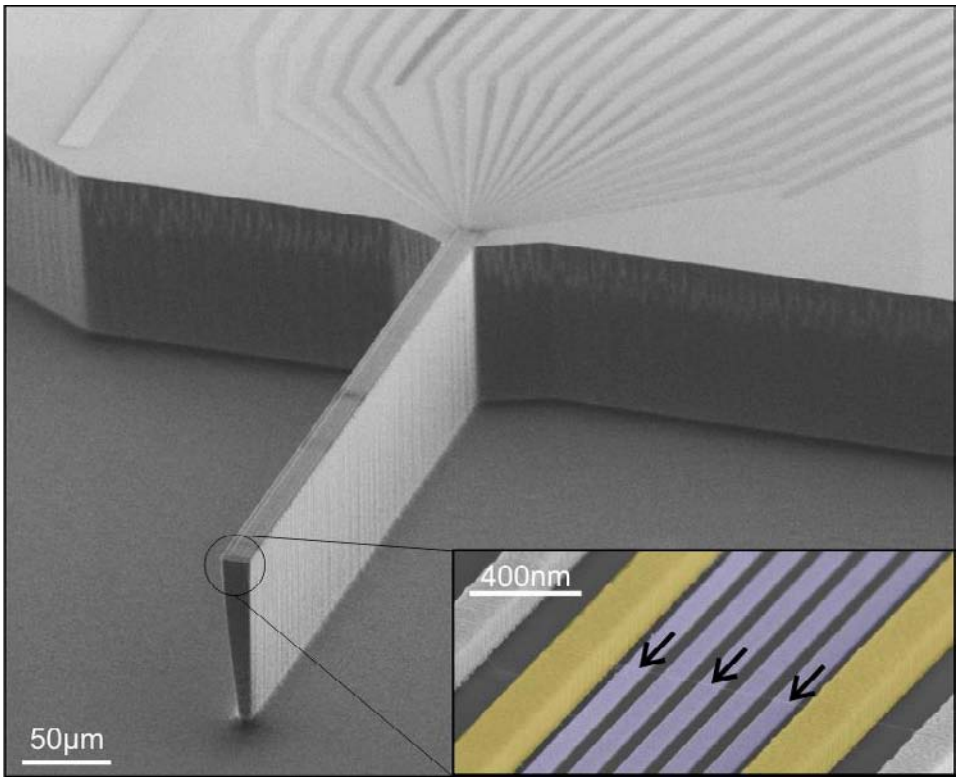

Figure S1. SEM image of a nanotube-based scanning SET device. Main panel: A zoom-out view of the deep-etched pillar, where near its leading edge (inset) an individual single-wall carbon nanotube is placed

(indicated by arrows). The nanotube touches source and drain contacts (yellow) and is suspended above five gates (blue). In the experiments in this paper all the gates are electrically chained together acting effectively as one large gate.

S2. Measurement scheme: disentangling mechanical and electronic contributions to the measured response

The SET senses the local vacuum potential, ϕ, above the LAO/STO surface, which is related to the energies of the system by (Fig S2a): $\phi = V_S + W$, where V_S is the electrochemical potential, set by a DC voltage source in our experiment, and W is the local workfunction. A change in either of these energies is reflected in a change in ϕ, which couples to the SET through the induced "control charge", $Q = C\phi$, modulating the measured current as: $\Delta I = g(C\Delta\phi + \phi\Delta C)$, where g is the "gain" of the SET and C is the capacitance between the nanotube and the surface.

The measurement circuit is outlined in Fig. S2b. To independently extract W, the vertical piezoresponse, $\frac{\partial Z}{\partial V_{BG}}$, and the lateral electromechanical response embedded in the electronic compressibility, $\frac{\partial \phi}{\partial V_{BG}}$, we exploit our ability to control the electrochemical potential directly with a voltage source, V_S. This voltage is applied by a surface contact to the 2DES and the back gate, such that its application would not influence the 2DES charge density, but only change the relative potential of the sample as a whole with respect to the SET. We then simultaneously measure the AC responses in the SET current to several different excitations applied at different frequencies. These include the response to an excitation of the nanotube-surface separation ($H_Z = \frac{\partial I}{\partial Z}$), the electrochemical voltage ($H_S = \frac{\partial I}{\partial V_S}$), and the back gate voltage ($H_{BG} = \frac{\partial I}{\partial V_{BG}}$). To extract the various physical quantities, we form the appropriate ratios of these responses as a function of V_S, normalizing out the detailed response characteristics of the SET "amplifier" and directly giving the required physical quantities, as is shown below.

DOI: 10.1038/NMAT3810

To obtain W, we normalize H_Z by H_S: $\frac{H_Z}{H_S} = \frac{1}{C}\frac{\partial C}{\partial z} \cdot (W + V_S) = a_Z V_S + b_Z$, which is a function that is linear in V_S. The coefficients a_Z and b_Z are obtained by a linear fit in V_S. We then find: $W = \frac{b_Z}{a_Z}$.

To obtain the piezoresponse, $\frac{\partial Z}{\partial V_{BG}}$, we normalize H_{BG} by H_S: $\frac{H_{BG}}{H_S} = \frac{1}{C}\frac{\partial C}{\partial V_{BG}}(W + V_S) + \frac{\partial \phi}{\partial V_{BG}} = a_{BG} V_S + b_{BG}$, which again is a linear function in V_S. Thus, we obtain the coefficients a_{BG} and b_{BG} by a linear fit in V_S. Combining these coefficients with those obtained above, we find the piezoresponse: $\frac{\partial Z}{\partial V_{BG}} = \frac{a_{BG}}{a_Z}$. The lateral electromechanical response is then embedded in the extracted electronic compressibility: $\frac{\partial \phi}{\partial V_{BG}} = b_{BG} - a_{BG} \cdot \frac{b_Z}{a_Z}$.

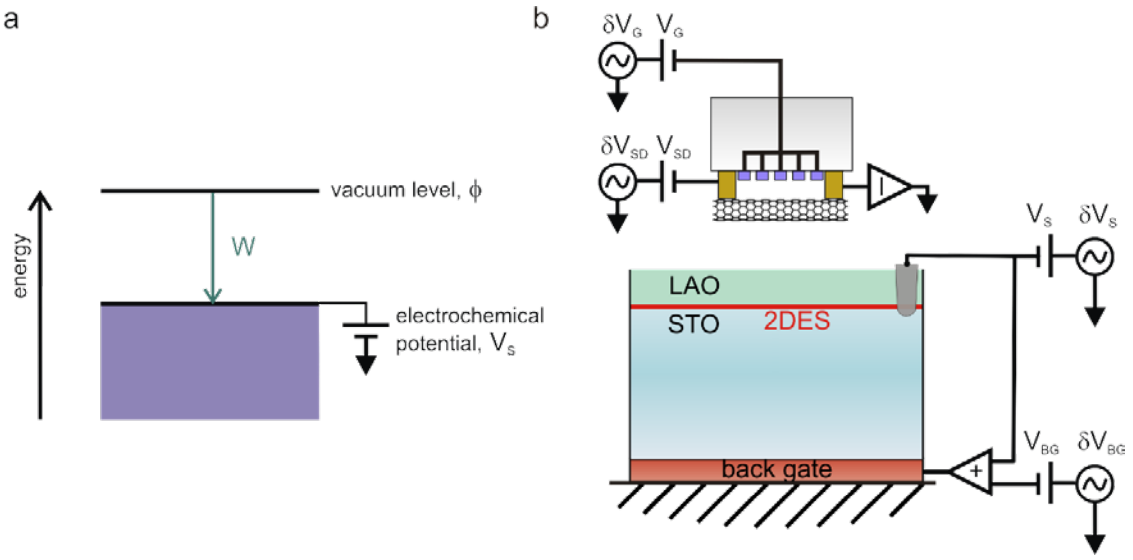

Figure S2: Scanning single electron transistor measurement scheme. a) Schematic of energetics at the LAO/STO interface. The vacuum level ϕ above the surface is sensed directly by the SET, and is related to the local workfunction W and the electrochemical potential V_S (set directly by an applied voltage in the experiment) by the equation: $\phi = V_S + W$. The shaded region represents the occupied charge states near the surface. b) Measurement circuit: The back-gate, interface, nanotube source contact (yellow, left) and nanotube gates (blue) are connected to DC sources (V_i) and AC sources (δV_i) at different frequencies in the range of 10's to 100's of Hz. The measured current at the NT drain (yellow, right) has AC components at identical frequencies, reflecting its coupling to each of these electrodes. Note that the voltage V_s is

connected to both the interface (through an ohmic contact shown in gray) and the back-gate, such that it determines the overall "sample" electrochemical potential. Not shown are three additional AC excitations that oscillate the position of the SET in the X,Y, and Z directions.

S3. Scanning SET spatial resolution

The spatial imaging resolution of the scanning SET is limited by two terms: the height of the SET above the sample and the dimensions of the electronic quantum dot formed in the suspended nanotube segment, which acts as the actual detector. The size of the quantum dot is set by the distance between the P-N junctions formed between the contact electrodes. These P-N junctions constitute the SET's tunnel barriers, and in general their separation is smaller than the lithographically-defined spacing between the contact electrodes, thus effectively making a smaller detector. The spatial resolution achieved in the measurements presented in this work is $\sim 600nm$, directly determined by the full width at half maximum of Gaussian fits to peaks in $d\phi/dV_{BG}$ at domain walls, shown in Figure S3.

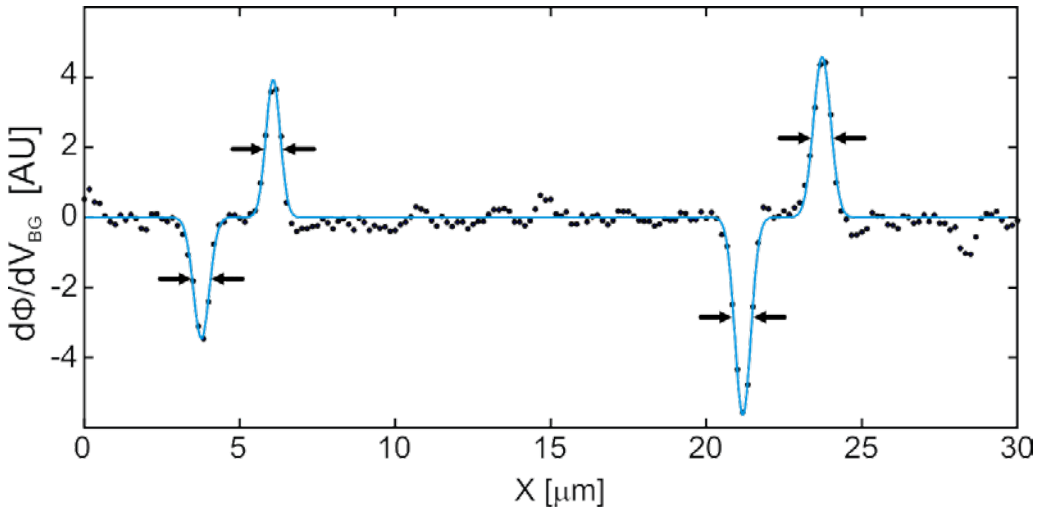

Figure S3: Scanning SET spatial resolution. The measured $d\phi/dV_{BG}$ (black dots) is plotted as a function of spatial coordinate across a series of domain walls. The scan is along the direction parallel to the nanotube axis, in which the resolution of the measurement is lower due to the finite length of the quantum dot detector formed in the nanotube along this direction. The solid blue line is a sum of a series of Gaussians fits to the peaks in $d\phi/dV_{BG}$. The full widths at half maximum (FWHM) of the Gaussians (arrows) are $600nm \pm 40nm$ giving directly the resolution of our scanning measurements.

DOI: 10.1038/NMAT3810

S4. Gate voltage dependence of piezoelectric response: asymmetry and hysteresis

Figure S4 shows the measured piezoelectric response, dz/dV_{BG}, as a function of the back-gate voltage for opposite sweep directions (arrows). The scans highlight two important phenomena related to domain motion: Firstly, dz/dV_{BG} is asymmetric around zero gate voltage – it is large at negative voltages and tends to zero at positive gate voltages. Secondly, around the two sharp transition regions in dz/dV_{BG} this quantity is hysteretic with respect to gate voltage sweep direction. However, the response as measured from voltage sweeps in the same direction is highly repeatable and shows no signs of 2DES depletion over the $400V$ gate voltage span.

The source of the asymmetry and hysteresis becomes clear from optical measurements performed on similar LAO/STO and bare STO samples[2–5] which provide a larger field of view and show domain structure over the entire sample at once. We observe that the asymmetry in piezoresponse is microscopically connected to different regimes of the domain motion at positive and negative gate voltages, as indicated at the top of figure S4. Note that these regimes appear after we have cycled at least once the back gate voltage to large values (see section S8 below), and are measured $\sim 400\mu m$ from the edge of the sample. At small positive and negative gate voltages we observe striped domain patterns that move strongly with varying gate voltage, which we term the "moving stripes" regime. At large positive gate voltages, domain patterns are still visible, but their motion decreases as the gate voltage is increased. Thus, at these voltages the diminishing piezoelectric response is explained by the absence of domain motion. This is the "fixed stripes" regime. At large negative gate voltages, the stripes retreat to the sample edges as the voltage is made more negative, and a mono-domain fills the image, which we term the "homogenous" regime. In this regime, the scanning field of view is free of domain walls, though beyond this window, the domain walls continue to retreat to the edge of the sample with increasingly negative gate voltage. Thus, the piezoresponse is still large in this regime due to domain motion outside of the field of view of the scanning SET.

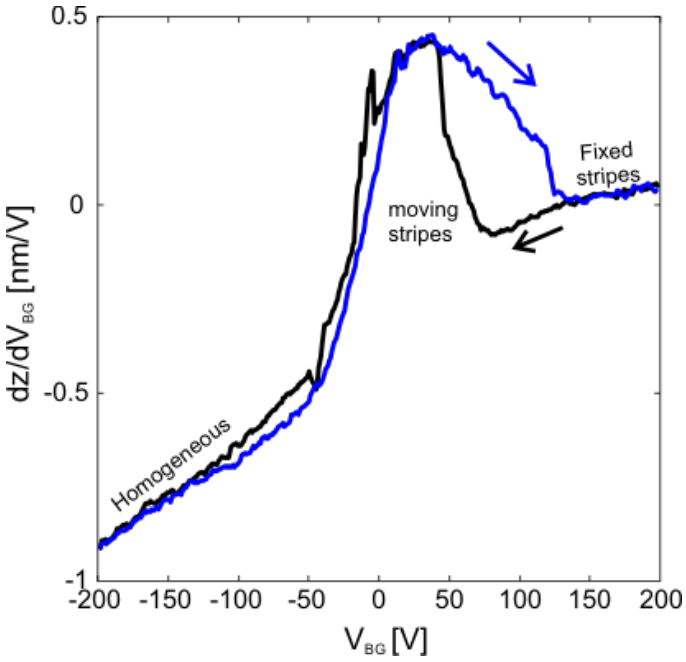

Figure S4: Piezoelectric hysteresis. Measured piezoelectric response, dz/dV_{BG}, as a function of V_{BG} for opposite sweep directions, indicated by arrows. The three domain regimes are labeled near the corresponding sections of the data.

S5. Maps of the surface electrostatic disorder potential and the domain-generated surface potential

Figure S5 shows the electrostatic potential measured as a function of position at a fixed back-gate voltage above the LAO/STO surface. The measurement is dominated by surface disorder which is $\sim 10-50mV$ in amplitude and invariant with respect to the gate voltage. The potential map in (a) is taken at a gate voltage where stripes are present (multiple domains), whereas the potential map in (b) is taken at a gate voltage where the field of view is homogenous (mono-domain). The difference between panels (a) and (b) is shown in (c). By taking differences between these potential maps, we reveal the underlying mV-scale potential stripes generated by the tetragonal STO domains. Compare directly with the potential map shown in Fig 5a in the main text.

We note that striped potential modulations can have a more significant impact on the 2DES than the disorder, despite the fact measured disorder is larger in magnitude.

DOI: 10.1038/NMAT3810

This is due to the fact that the measured disorder potential reflects disorder above the 2DES at the interface, arising from surface absorbents and disorder within the LAO. This bare surface potential will then be substantially screened at the LAO/STO interface by the 2DES. In contrast, the measured striped potential is a measurement of the screened potential modulation at the LAO/STO interface. Thus, from the perspective of the 2DES, the striped potential modulations can be much larger in magnitude.

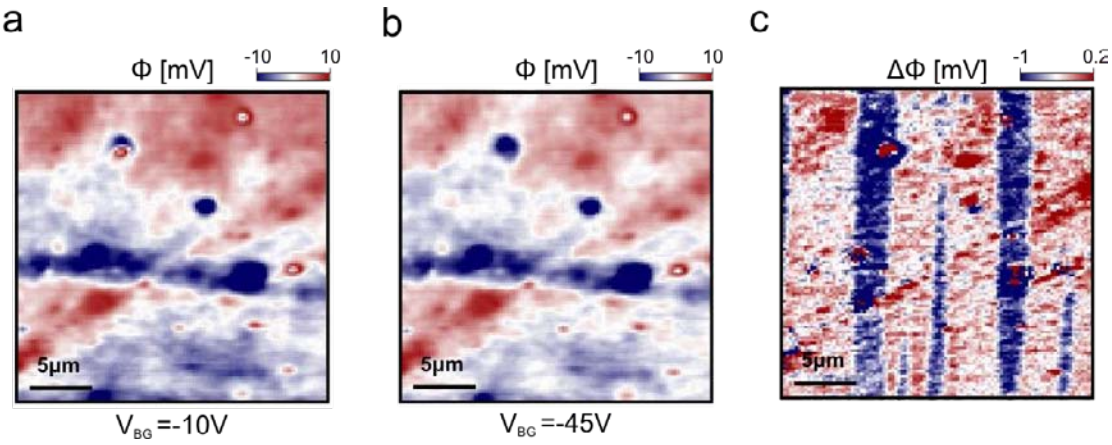

Figure S5. Measured maps of the electrostatic disorder potential and their difference giving the domain-generated surface potential. a-b) Electrostatic potential maps measured at $V_{BG} = -10V, -45V$. c) The difference between the data in panels (a) and (b). Since in panel (b) the entire field of view is occupied by a mono-domain, this difference map subtracts the disorder potential that is gate-voltage independent, allowing observation of the small potential modulations due to the striped domains present in panel (a) but hidden beneath the large disorder. The red 45^{O} streaks that are still visible in (c) are artifacts due to imperfect subtraction between (a) and (b). Such artifacts can arise from small, uncompensated gating differences of the SET by the back gate between images taken at such different gate voltages. It should also be stressed that in our studies we could not identify a clear influence of the point-like disorder features (like those observed *e.g.* in this figure) on the domain dynamics.

S6. Optical images of domains: temperature and gate-voltage dependence

Figure S6a-b show measured optical images[2–5] in a bare STO sample measured at temperatures above the ferroelastic transition ($T = 110K$, Fig. S6a) and below the transition ($T = 70K$, Fig. S6b). The appearance of a striped pattern of domains similar in dimension and orientation to that observed in the scanning SET experiments is nicely

correlated with the crossing of this transition. We observe identical results in several LAO/STO and bare STO samples. Fig S6c shows a series of line cuts taken along the dashed orange line of S6b as a function of temperature. Red corresponds to higher optical intensity, whereas blue corresponds to lower optical intensity. For temperatures above the ferroelastic transition ($T = 105K$, marked by the black dashed line), there are no stripes in the image, indicating that the STO crystal is cubic. The stripes appear as the temperature drops below the transition, establishing that they arise from the STO ferroelastic transition to tetragonal crystal symmetry[3]. No other structural transitions are observed as the temperature is further lowered[6], though the lack of observation may be due to limitations of the optical setup.

Fig. S6d shows a diagram of the stripe mobility created from a collection of optical images of an LAO/STO sample. The mobility of the stripes is observed to be strongly temperature dependent. In the lower, gold region of the plot, the stripes are visible, but are immobile. As the gate voltage is made more negative and the temperature is lowered, the stripes become mobile, and we move into the "moving stripes" phase shown in green. As the gate voltage is made more negative still, or the temperature further lowered, the stripes retreat to the sample edges, and the center of the sample becomes homogenous with a mono-domain, shown in blue. This increasing domain wall mobility with decreasing temperature is consistent with the temperature dependence of the piezoelectric response measured by Grupp *et al*. (Reference 12 in main text).

DOI: 10.1038/NMAT3810

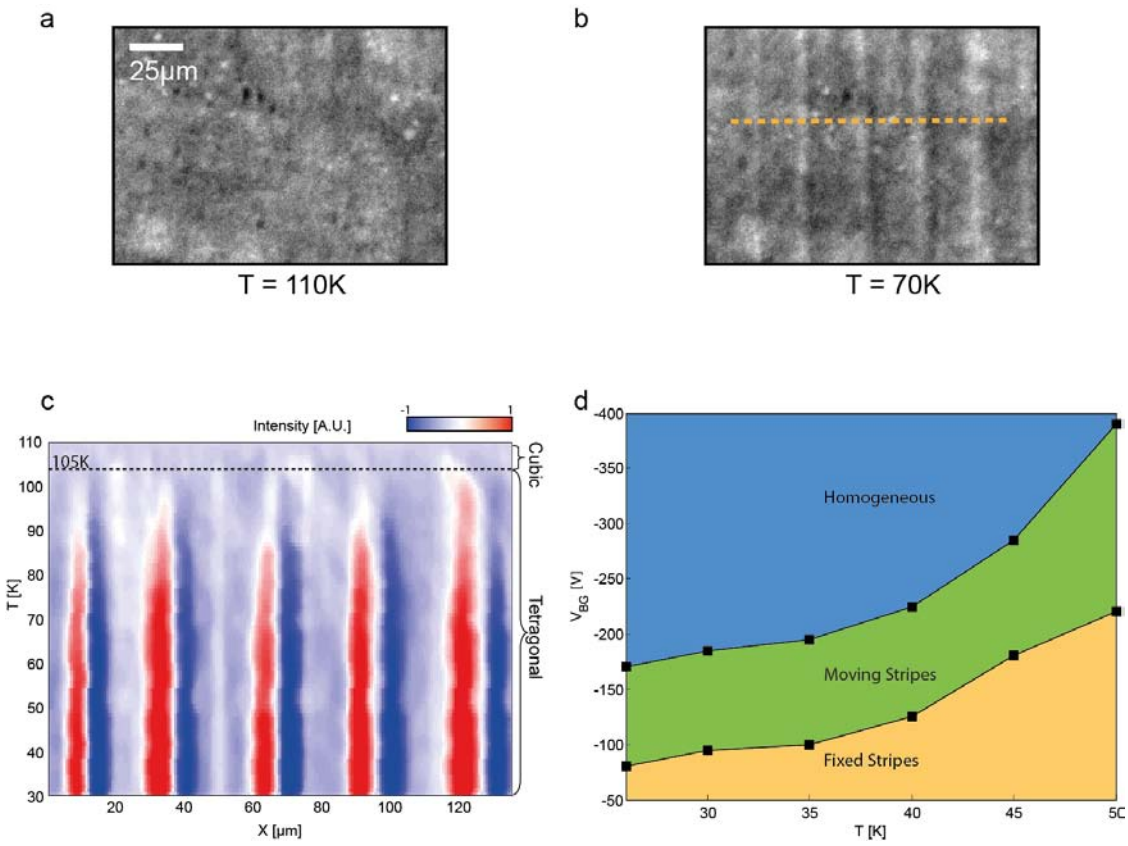

Figure S6: Temperature dependence of stripes. a,b) Optical images of bare STO. An image taken above the ferroelastic transition temperature (a) shows no stripes, while an image taken below the ferroelastic transition temperature (b) shows stripes[2–5]. c) Line cuts taken along the orange dashed line in (b) as a function of temperature. The stripes appear as the temperature drops below $T = 105K$, firmly establishing that they arise from the STO ferroelastic transition to tetragonal crystal symmetry[7]. d) A diagram of the stripe mobility created from a large set of optical images. The mobility of the stripes is observed to be strongly temperature dependent[8], increasing as the temperature is lowered and the gate voltage is made more negative. We find nice correspondence with the phase diagram measured in Ref 9 which used neutron diffraction.

S7. Side view optical image of domains spanning entire sample thickness

Figure S7 presents a cross-section of bare STO imaged via cross-polarized optical microscopy at $T = 30K$ (below the ferroelastic transition temperature). We clearly see the X and Z domains separated by boundaries that penetrate the bulk of the STO at 45° angles (0° and 90° when viewed from above), many of which persist completely from top

to bottom of the sample. Here we use the same domain labeling convention as explained in Fig. 3 of the main text.

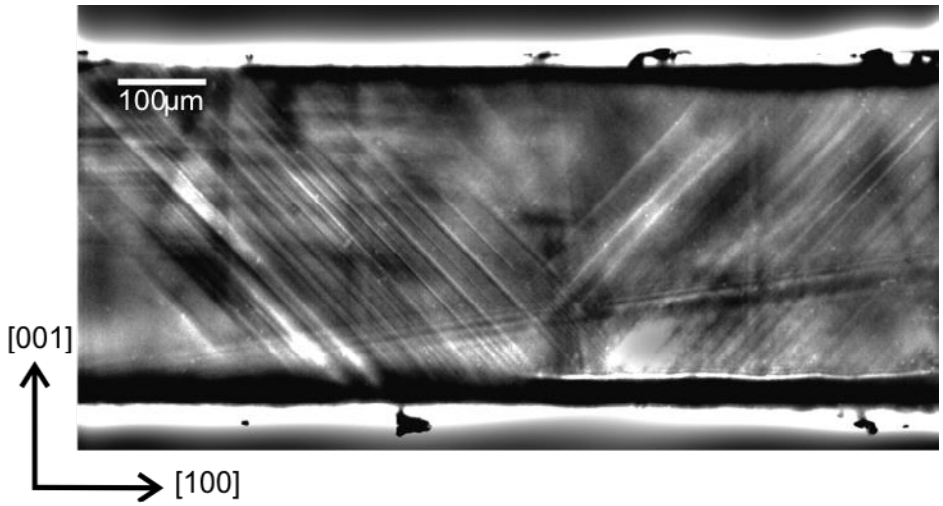

Figure S7: Side view optical image of bare STO at T=30K. The side plane of the sample is polished to allow viewing domain structure. Sample thickness is $500\mu m$. Bright top and bottom stripes in the figure correspond to the top and bottom planes of the sample. Clearly visible are 45° angled lines, which appear only below the ferroelastic transition temperature. On the contrary, the nearly vertical and horizontal lines are independent of temperature and correspond to scratches on the side surface.

S8. The dependence of domain distribution on initial voltage cycling post cooldown

In this section we show that the way in which the gate voltage is cycled after cooldown can be detrimental to the prevalence of striped domains in the sample. While as-cooled samples and those that are only cycled to small back-gate voltages remain covered with striped domains over their entire areas, if the back-gate voltage is cycled even once to a high enough voltage, the stripes can be cleared from the bulk of the sample, leaving only narrow sections of varying domains along the sample edges.

Upon cooling below the ferroelastic transition temperature, stripes appear distributed haphazardly over the entirety of the samples, emanating from their edges. After cycling the gate voltage, typically through hundreds of volts applied across the $\sim 500\mu m$ thick STO, we obtain repeatable gate-voltage dependent domain distributions[5]. Such gate voltage cycling can also clear the stripes entirely from the central areas of the

DOI: 10.1038/NMAT3810

samples and leave them only in a strip within a few hundreds of microns from the edges[10]. This phenomenology is summarized in Fig S8. Here, we cycle an LAO/STO sample at $T = 30K$ from zero volts on the back gate to negative gate voltages and then back to zero, and we repeat this procedure several times, each time increasing the magnitude of the negative voltage. Cycling to $V_{BG} = -50V$ and then back to $V_{BG} = 0V$ does not noticeably influence the domain distributions. However, increasing the cycling up to $V_{BG} = -100V$ clears some domains near the center of the sample (region enclosed by the yellow dashed line) even when the voltage is returned to $V_{BG} = 0V$. Cycling up to $V_{BG} = -200V$ and back to $V_{BG} = 0V$ leaves the sample free of domain walls except for strips within $\sim 100 - 200\mu m$ from the edges (more generally can be within $100 - 500\mu m$ from the edges depending on sample-specific details).

Although we observed identical domain behavior in all measured samples, we note that the domain dynamics are temperature dependent (Supplementary S6), should depend on built-in strain and specific sample growth conditions, and also may be different near patterned features. These aspects should be carefully tested in future transport experiments carried out in conjunction with direct observation of domain dynamics.

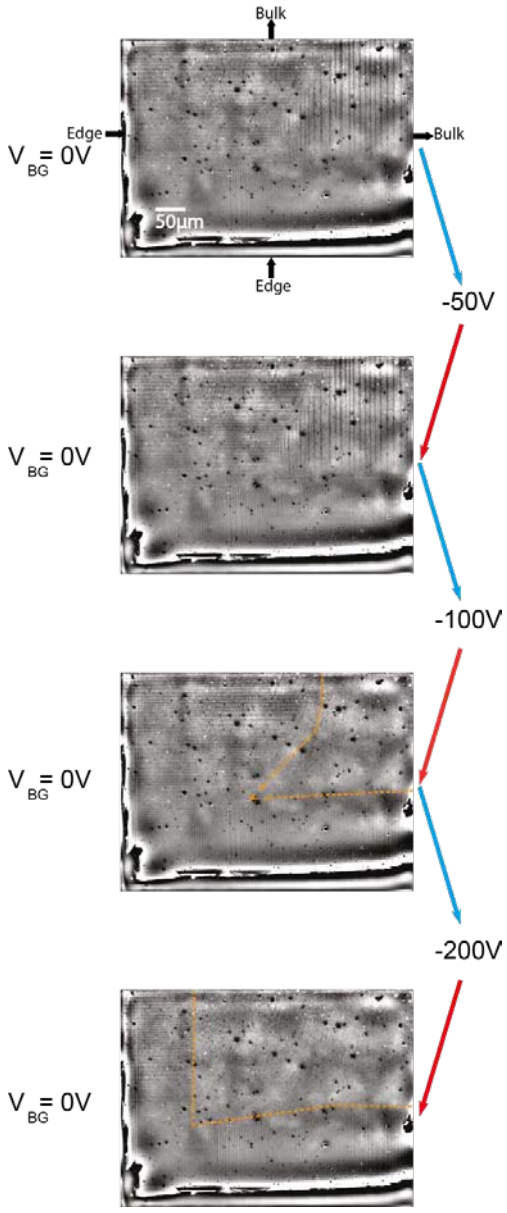

Figure S8: The dependence of domain distribution on initial voltage cycling post cooldown. Optical images of an LAO/STO sample at $T = 30K$ as it is cycled from zero gate voltage post-cooldown to negative voltages and back to zero, increasing the magnitude of the negative voltage with each iteration (arrows on the right). Before voltage cycling, stripes are distributed haphazardly throughout the sample (top panel). Cycling the gate voltage to $V_{BG} = -50V$ and back to $V_{BG} = 0V$ does not noticeably influence the domain distribution (2nd panel from top). Cycling the gate voltage up to $V_{BG} = -100V$ and back to $V_{BG} = 0V$ begins to clear stripes from the bulk of the sample (region bounded by dashed orange line, 2nd panel from bottom), and cycling up to $V_{BG} = -200V$ and back to $V_{BG} = 0V$ clears stripes everywhere except for near the edges (bottom panel).

DOI: 10.1038/NMAT3810

S9. Comparison between samples from different suppliers and with different surface treatments

To investigate how general are our observations regarding the voltage dependence of the domain structure, we performed optical measurements across a variety of different samples. In addition to two different LAO/STO samples, we also studied several bare STO(100) samples obtained from different substrate suppliers (Crystec, MTI) which underwent different surface treatments (untreated vs. TiO_3-terminated surfaces created via step-etching and thermal annealing).

Across all samples, we observed a rather universal dependence of the domain landscape upon gate voltage cycling: the as-cooled samples (before the application of any gate voltage) have their entire area densely covered by differently-oriented domains that appear at the ferroelastic transition temperature and maintain the same landscape when the sample is cooled further to lower temperatures. Upon cycling the relative voltage between the back gate and the surface to high values and then back to zero, we observe that in all cases 0° and 90° domain wall patterns (between x/z and y/z domains, respectively) retreat toward the edges of the samples, leaving the centers free of these domain walls, even when the gate voltage is returned to zero. This behavior is demonstrated for three different samples (LAO/STO, TiO_3-terminated STO from Crystec, untreated STO from MTI) in Figure S9 below. The left panels show the pattern of domains before voltage cycling (as-cooled), and as can clearly be seen the domain wall patterns cover the entire field of view in the figure (in all cases they cover the entire area of the sample, not shown). The right panels show the domain landscape after cycling to $V_{BG} = +200V$ and back to $V_{BG} = 0V$. In all cases the 0° and 90° domain walls shrink to be confined within only a short distance from the sample edge, as indicated by the orange lines which mark the boundary where these patterns terminate. Note that the additional (voltage-cycling-independent) structure in the sample in panel S9b is due to surface contamination, and that in the MTI sample (untreated, bare STO(100)) in panel S9c, the signal from domain walls between x/y domains (45°) that originates deep below the surface is very strong and remains dominant when the focus is on the surface. Small patches of x/z domain walls still remain in this sample after voltage cycling.

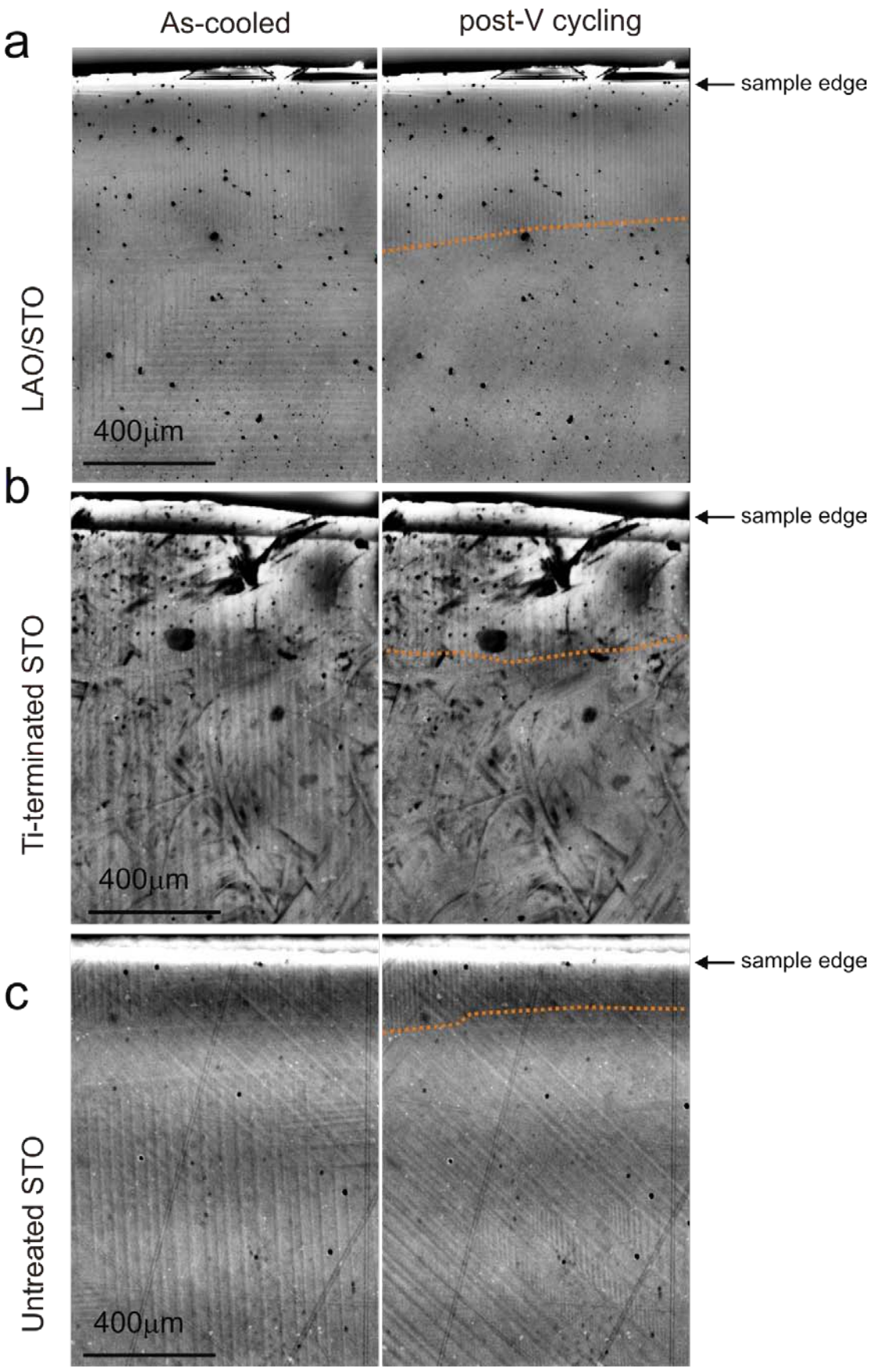

DOI: 10.1038/NMAT3810

Figure S9: Images of domains as-cooled and post-voltage cycling in several different samples. Each panel presents a different sample, before (left) and after (right) voltage cycling. a) 5 unit cell LAO/STO sample. b) TiO_3-terminated STO(100) from Crystec. The titanium surface termination is achieved through an etch process, followed by thermal annealing. c) Untreated, as-grown STO(100) from MTI Corporation. In all panels the edge of the sample appears at the top of the image (black arrow). The dashed orange lines mark the boundaries of the regions cleared of x/z and y/z domain walls after voltage cycling of the back gate. The spatial scale is identical in all images. The STO thickness in all cases is $500\mu m$. The visible smudges in panel (b) are due to dirt that condensed on the sample surface during one of the cooldowns, which is temperature and gate-voltage independent, and unrelated to the underlying domains. In the untreated STO sample in panel (c), 45° domain boundaries between x/y domains gave an especially strong signal as compared with the other two samples. These 45° domain boundaries are usually seen when the focal plane is deep below the sample surface, whereas at the surface only the 0° and 90° x/z and y/z domain walls are typically visible. In this sample the signal of the deeper 45° domain boundaries was so strong that it had significant visual imprint even when the focal plane was at the surface of the sample.

S10. Transport and capacitance characterization of the 2DES of the studied LAO/STO sample

To support the notion that our sample is typical of those used in other studies, we have further characterized the LAO/STO sample on which the scanning SET measurements were made by performing a series of transport and capacitance measurements. Magnetotransport measurements were performed utilizing the Van der Pauw method to extract the mobility and carrier density of the 2DES, and the capacitance between the 2DES and the back gate was also measured as a function of gate voltage.

After voltage cycling, at $V_{BG} = +200V$ the carrier density of the 2DES was $2.2 \pm 0.1 \times 10^{13} cm^{-2}$, with mobility $660 \pm 10\, cm^2/Vs$. The sheet resistance as a function of gate voltage is shown in figure S10a. At the highest 2DES density ($V_{BG} = +200V$), this sheet resistance is lowest at a value of 400 Ω/□. As the gate voltage is made more negative and the 2DES is depleted, the sheet resistance increases to the value of 6000 Ω/□ at $V_{BG} = -200V$.

The capacitance between the 2DES and the back gate is plotted as a function of voltage in figure S10b. The capacitance is peaked around zero gate voltage where the

dielectric constant of the STO is highest. Because the STO dielectric constant decreases with increasing applied field, the capacitance drops as the gate voltage is swept away from zero in either direction. We note that the peak in capacitance is always located near zero voltage, independent of voltage cycling history. This suggests that oxygen migration plays a minimal role in our cryogenic measurements. Were oxygen migration to occur as a result of voltage cycling, we would expect the resulting oxygen vacancies to act as an effective gate voltage, shifting the peak in capacitance away from zero volts, which we do not see in our measurements.

Overall, these trends in transport and capacitance compare favorably to such measurements in other LAO/STO studies, supporting the relevance of the domain physics uncovered in this work to other 2DES systems built upon STO.

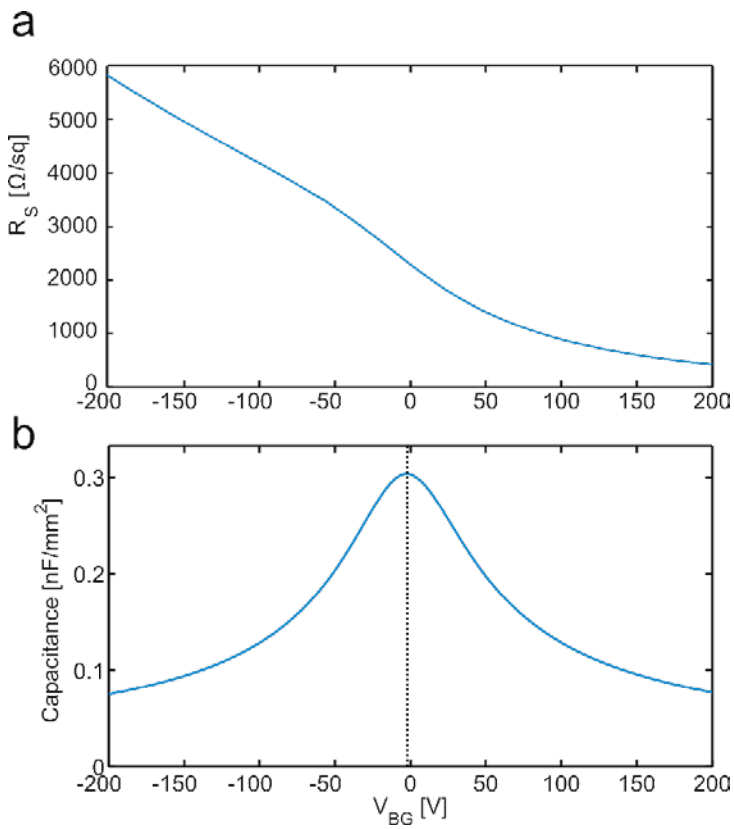

Figure S10: LAO/STO 2DES characterization: sheet resistance and capacitance. a) Sheet resistance of the 2DES as a function of back gate voltage after voltage cycling for the 6 unit cell LAO/STO sample used for SET imaging in the main text. The resistance steadily increases as the gate voltage is made more

DOI: 10.1038/NMAT3810

negative, depleting the 2DES electron density. b) Capacitance of the same sample as a function of back gate voltage post voltage cycling. The peak capacitance is marked by a dashed vertical line.

S11. Surface potential and 2DES density modulation

In this section, we explain the connection between the local surface potential variation measured by the SET and the corresponding density modulation in the 2DES. In principle, the surface of two neighboring but separated domains (depicted schematically as A and B in Fig. S11a) may have different electrochemical potentials, *e.g.* due to changes of the 2DES energy bands with mechanical stretching along different directions. If these two domains are in electrochemical equilibrium (their natural state when in contact, Fig S11b) they must have the same electrochemical potential. This equilibrium is achieved by charge transferring across the domain wall, forming a dipole-like charge distribution at the wall that generates a step in the local vacuum level. This potential step exactly compensates the workfunction difference, $\Delta\phi = W_A - W_B$, thereby flattening the electrochemical potential across the domains (Fig S11b). This step in the local vacuum potential across domain walls is the quantity measured in our scanning SET experiment.

The amount of density modulation in the dipole-like charge double layer in the 2DES is estimated from simple electrostatics. As this charge redistribution is restricted to 2D whereas the field lines propagate from one domain to its neighbor in 3D, the charge density will decay as one over the distance from the domain wall: $\Delta n \sim \epsilon \Delta\phi / ed$, where ϵ is the dielectric constant, e is the electron charge, and d is the distance from the domain wall (Fig S11c). Thus for lengthscales on the order of typical ferroelastic domain wall thickness $\sim 1 - 10nm$ and an $\epsilon \sim 1000 \cdot \epsilon_0$, which would correspond to the reduced dielectric constant of STO in the high field region near the interface, we find $\Delta n \sim 0.5 - 5 \cdot 10^{12} cm^{-2}$. This would be a significant fraction of the average charge density in the 2DES.

We note that above we consider only the simplest and most generic mechanism for charge modulation in the system induced by the potential modulation. Other, more

speculative scenarios that include strain effects on the LAO and charge redistribution between internal degrees of freedom in the system (e.g. between different subbands of the 2DES) may also be at play. Such mechanisms could contribute additional channels for creating significant modulation to the 2DES density in excess of the mechanism discussed above.

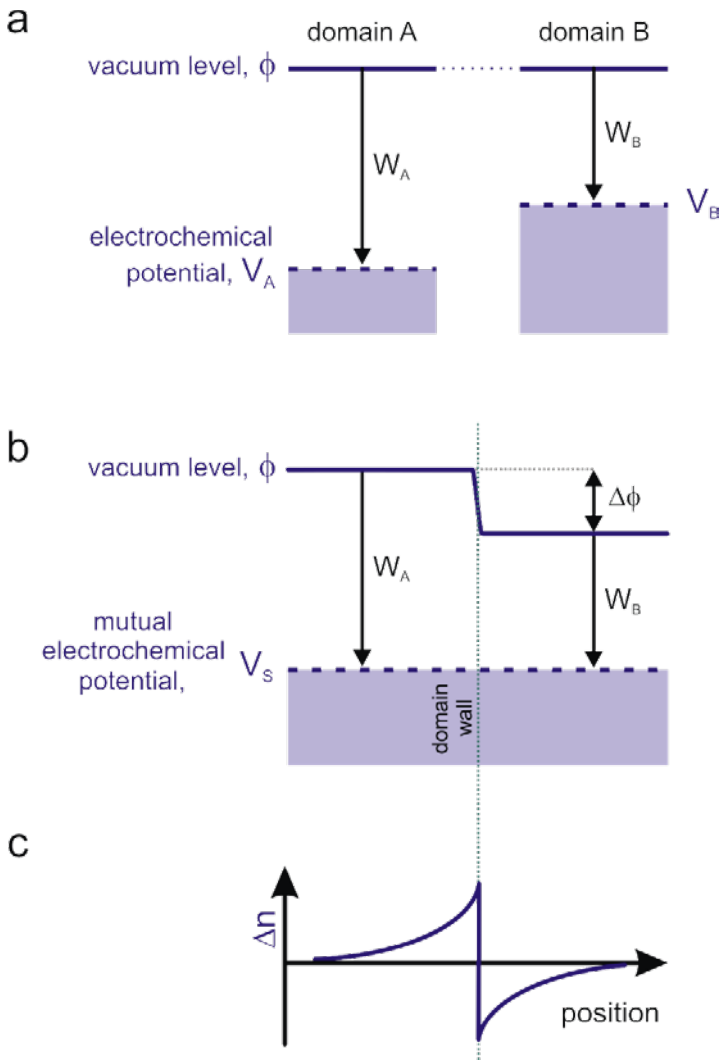

Figure S11: Potential and charge modulation across a domain wall. a) Separated domains A and B may have 2DES with different electrochemical potentials V_A and V_B, respectively, due to strain-induced changes to the 2DES bandstructure, resulting in differing workfunctions W_A and W_B. b) When in contact, the domains reach equilibrium by transferring charge across the domain wall to maintain a constant value of the electrochemical potential, V_S. This generates a step (contact potential) in the vacuum potential, ϕ,

DOI: 10.1038/NMAT3810

equal to the difference in workfunctions: $\Delta\phi = W_A - W_B$. c) The corresponding charge density modulation that creates this contact potential is dipole-like, falling off as one over the distance from the domain wall, since the charge redistribution is confined to 2D whereas the field lines between domains permeate the entire 3D volume.

References

1. Waissman, J. *et al*. Realization of pristine and locally tunable one-dimensional electron systems in carbon nanotubes. *Nature Nanotechnology*, **8**, 569–574 (2013).

2. Sawaguchi, E., Kikuchi, A. & Kodera, Y. Microscopic Examination of SrTiO3 at Low Temperatures. *J. Phys. Soc. Japan;* **18**, 459–60 (1963).

3. Lytle, F. W. X-Ray Diffractometry of Low-Temperature Phase Transformations in Strontium Titanate. *Journal of Applied Physics* **35**, 2212 (1964).

4. Chang, T. S. Direct Observation Of Single-Domain SrTiO3. *Applied Physics Letters* **17**, 254 (1970).

5. Buckley, A., Rivera, J. P. & Salje, E. K. H. Twin structures in tetragonal SrTiO3: The ferroelastic phase transition and the formation of needle domains. *Journal of Applied Physics* **86**, 1653 (1999).

6. Ang, C., Scott, J., Yu, Z., Ledbetter, H. & Baptista, J. Dielectric and ultrasonic anomalies at 16, 37, and 65 K in SrTiO3. *Physical Review B* **59**, 6661–6664 (1999).

7. Müller, K., Berlinger, W. & Waldner, F. Characteristic Structural Phase Transition in Perovskite-Type Compounds. *Physical Review Letters* **21**, 814–817 (1968).

8. Scott, J., Salje, E. & Carpenter, M. Domain Wall Damping and Elastic Softening in SrTiO3: Evidence for Polar Twin Walls. *Physical Review Letters* **109**, 187601 (2012).

9. Sidoruk, J. *et al*. Quantitative determination of domain distribution in SrTiO3-competing effects of applied electric field and mechanical stress. *Journal of physics. Condensed matter* **22**, 235903 (2010).

10. Dec, J., Kleemann, W. & Itoh, M. Electric-field-induced ferroelastic single domaining of SrTi18O3. *Applied Physics Letters* **85**, 5328 (2004).

11. Ilani, S. *et al*. The microscopic nature of localization in the quantum Hall effect. *Nature* **427**, 328–332 (2004).

12. Eisenstein, J., Pfeiffer, L. & West, K. Negative compressibility of interacting two-dimensional electron and quasiparticle gases. *Physical review letters* **68**, 674–677 (1992).

13. Li, L. *et al*. Very large capacitance enhancement in a two-dimensional electron system. *Science* **332**, 825–8 (2011).

DOI: 10.1038/NMAT3810

14. Popovic, Z. S., Satpathy, S. & Martin, R. M. Origin of the Two-Dimensional Electron Gas Carrier Density at the LaAlO3 on SrTiO3 Interface. *Phys. Rev. Lett.* **101**, 256801 (2008).

15. Kalisky, B. *et al*. Locally enhanced conductivity due to the tetragonal domain structure in LaAlO3/SrTiO3 heterointerfaces. *Nature Materials* advance online publication, (2013) (DOI 10.1038/nmat3753).

16. Liu, M., Finlayson, T. & Smith, T. High-resolution dilatometry measurements of SrTiO3 along cubic and tetragonal axes. *Physical Review B* **55**, 3480–3484 (1997).

17. Pentcheva, R. *et al*. Parallel Electron-Hole Bilayer Conductivity from Electronic Interface Reconstruction. *Physical Review Letters* **104**, 166804 (2010).

18. Bell, C. *et al*. Dominant Mobility Modulation by the Electric Field Effect at the LaAlO3/SrTiO3 Interface. *Physical Review Letters* **103**, 25–28 (2009).

19. Santander-Syro, A. F. *et al*. Two-dimensional electron gas with universal subbands at the surface of SrTiO3. *Nature*, ***469***, 189–193 (2011).